2021-03

Assessing focused wave impacts on floating WECs using OpenFOAM

Brown, Scott Andrew

10.1680/jencm.19.00036
Proceedings of the Institution of Civil Engineers: Engineering and Computational Mechanics
Thomas Telford

Proceedings of the Institution of Civil Engineers
Pages 1–12

Keywords: Renewable Energy, Fluid Dynamics, Computational Mechanics

ice | proceedings

Assessing focused wave impacts on floating WECs using OpenFOAM

S. A. Brown, E. J. Ransley and D. M. Greaves
School of Engineering, Computing and Mathematics, University of Plymouth, Drake Circus, Plymouth, UK, PL48AA

The presented work considers focused wave interactions with floating wave energy converters (WECs) and represents an individual contribution to the CCP-WSI Blind Test Series 2, in which the submitted results are compared against both physical and alternative numerical solutions for varying wave steepness achieved through changes in peak frequency. Reducing the time taken to provide reliable results is critical if computational fluid dynamics (CFD) is to become a routine design tool for offshore renewable energy devices. This can potentially be achieved by simplifying simulation setup, and hence reduce the required man-hours, through standardised 'best practice' procedures. In order to achieve this, it is essential that the limitations of a numerical tool are well understood, and minimised. Therefore, this study aims to quantify the numerical reproduction of the focused wave event, and the motion of two different geometries predicted using a commonly used CFD methodology with waves generation achieved via linear superposition. The results imply that the error in peak values of heave and empty tank surface elevation are comparable, but the peak surge and pitch are substantially larger. This is likely due to a combination of numerical modelling errors, which must be addressed in future work.

1. Introduction

Uncertainty in the accuracy of numerical solutions is one of the key issues that is limiting the use of computational fluid dynamics (CFD) as a routine design tool, along with the time taken to obtain reliable results. The time taken to run a simulation is notoriously large, but this can be countered through use of a larger computational resource, which is becoming increasingly readily available. However, an often-overlooked factor is the number of man-hours required to setup a case through processes such as mesh design (Schmitt *et al.*, 2012), which, from experience, is potentially larger than the simulation time. For industry to benefit from the high volume of information that CFD models can provide, the setup process must be streamlined, and one way that this could be achieved is through parametric understanding of numerical accuracy and providing standardised, 'best practice' procedures. An ever-expanding use of CFD simulations for wave-structure interaction (WSI) applications (Windt *et al.*, 2018b; Palm *et al.*, 2016; Devolder *et al.*, 2018), has led to preliminary studies seeking to set the foundations for standardisation, such as: the expansion of mesh convergence schemes to estimate uncertainty (Eskilsson *et al.*, 2017; Wang *et al.*, 2018); assessment of available wave generation methods (Windt *et al.*, 2019b); the influence of mesh deformation scheme (Windt *et al.*, 2018a); and turbulence modelling under breaking waves (Brown *et al.*, 2016). However, in general, there are very few established guidelines for design of WSI CFD simulations. Bearing in mind the enormous number of techniques and settings available to a user, it is therefore neither uncommon, nor unexpected, to see a wide range of solutions for a single problem where the desired solution is not known *a priori*, even when applying the same base CFD code (Ransley *et al.*, 2019, 2020a).

In order to establish standard practices, it is essential that the limitations of a numerical tool are well understood, and minimised. Therefore, this study aims to quantify the numerical accuracy of a commonly used CFD methodology for assessing the interaction of focused wave events with a simplified floating WEC, building upon work conducted for a fixed structure (Brown *et al.*, 2019). The scope of this work is to compare a 'blind' estimation of numerical accuracy, based purely on the reproduction of empty tank data, with the observed error in the structure's motion following the release of the physical data. The work represents an individual contribution to the CCP-WSI Blind Test Series 2 (CCP-WSI, 2019), in which the submitted results are compared against both physical and alternative numerical solutions for varying peak wave frequency. The numerical results are obtained using the open-source C++ libraries of OpenFOAM v.5.0 (Weller *et al.*, 2017) to solve the Reynolds-Averaged Navier-Stokes (RANS) equations. Wave generation is achieved via linear superposition of first order wave components, derived from the empty tank data, and the

ID	mass [kg]	$z_{com,rel}$ [m]	draft [m]	I_{xx} [kgm^2]	I_{zz} [kgm^2]
Geometry 1	43.674	0.191	0.322	1.620	1.143
Geometry 2	61.459	0.152	0.330	3.560	3.298

Table 1. Structures considered in CCP-WSI Blind Test Series 2.

ID	ka [-]	h [m]	A_n [m]	f_p [Hz]	H_s [m]	L_c [m]
Wave 1	0.129	3.000	0.250	0.358	0.274	11.34
Wave 2	0.161	3.000	0.250	0.400	0.274	9.407
Wave 3	0.193	3.000	0.250	0.438	0.274	7.985

Table 2. Wave conditions used in CCP-WSI Blind Test Series 2.

relaxation zone method from the waves2Foam toolbox is used for absorption (Jacobsen *et al.*, 2012). Two different geometries are considered: a hemispherical-bottomed buoy; and a cylindrical structure with a moon-pool (Figure 1). For both structures, the effect of wave steepness on the surge, heave and pitch motion of the structure, caused by varying peak wave frequency, is examined.

2. CCP-WSI Blind Test 2 Case Studies

CCP-WSI Blind Test Series 2 concerns the response of floating surface-piercing structures, representing simplified WECs, to focused wave events varied in steepness through changes in peak frequency (CCP-WSI, 2019). Two different structures are considered: Geometry 1 is a hemi-spherical bottomed buoy 0.5 m in diameter, 0.5 m in height (Figure 1a); Geometry 2 is also 0.5 m in height but is a 0.577 m diameter cylinder with a 0.289 m diameter moonpool (Figure 1b). Both geometries are moored using the same linear spring mooring with stiffness 67 N/m and a restlength of 2.199 m, attached at the centreline, and bottom of the structure ($\times$ in Figure 1). The geometries have similar draft and water-plane area but the remaining properties are different (Table 1). Geometry 2 has larger mass; lower centre of mass ($+$ in Figure 1); and larger moment of inertia. Three focused wave events are considered with varying steepness ranging from $ka = 0.129$ to $ka = 0.193$ (Table 2). The steepness is changed by altering the peak frequency, f_p (and hence the characteristic wavelength L_c), whilst keeping the water depth ($h = 3$ m), amplitude ($A_n = 0.25$ m), and significant wave height ($H_s = 0.274$ m) constant (Table 2).

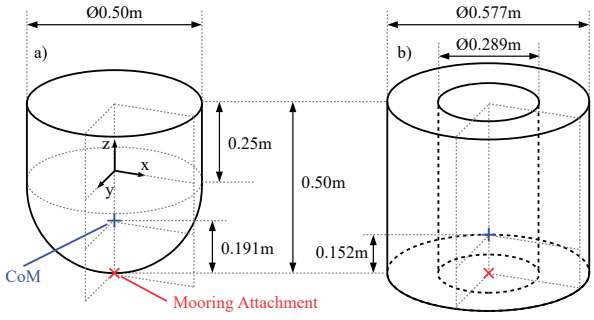

Figure 1. The two geometries from CCP-WSI Blind Test Series 2: Geometry 1 (a) is a hemispherical-bottomed buoy; Geometry 2 (b) is a cylindrical structure with a moonpool.

3. Numerical Model

This work utilises high-fidelity CFD due to its applicability in very high steepness nonlinear wave conditions (as experienced in focused wave events) and its capability to capture non-linear effects (e.g. green water) that may occur during the wave-structure interaction. The basis of the model is the open-source libraries provided by OpenFOAM (Weller *et al.*, 2017), and a version of the `interFoam` solver (Rusche, 2002), which has been modified for wave generation, and solves the two-phase, incompressible, Reynolds-Averaged Navier-Stokes (RANS) equations

$$\frac{\partial(\rho\mathbf{u})}{\partial t} + \nabla\cdot(\rho\mathbf{u}\mathbf{u}) = -\nabla p + \nabla^2(\mu\mathbf{u}) + \rho\mathbf{g}, \tag{1}$$

$$\nabla\cdot\mathbf{u} = 0, \tag{2}$$

where p is the pressure, $\mathbf{u} = (u, v, w)$ is the fluid velocity and $\mathbf{g}$ is acceleration due to gravity (Rusche, 2002). The fluid density, ρ, and dynamic viscosity, μ are determined using the volume of fluid (VOF) interface capturing scheme

$$\frac{\partial\alpha}{\partial t} + \nabla\cdot(\mathbf{u}\alpha) = 0, \tag{3}$$

$$\rho = \rho_1\alpha + \rho_2(1-\alpha), \tag{4}$$

$$\mu = \mu_1\alpha + \mu_2(1-\alpha), \tag{5}$$

where α is an indicator function representing the phase fraction of each mesh cell, and subscripts 1 and 2 represent air and water, respectively (Rusche, 2002). As explained by Rusche (2002), the `interFoam` solver uses an artificial compression term (C_α) when solving the transport equation for the volume fraction (equation 3), and this is set to $C_\alpha = 1$ in the present study. The Navier-Stokes equations (equations 1 and 2) are solved using a first order temporal scheme (Backwards Euler) and second order spatial schemes (Central Differencing and MUSCL). A variable timestepping approach has been utilised based on a maximum Courant number of 0.5, with the pressure-velocity coupling achieved via the Pressure Implicit with Splitting of Operators (PISO) algorithm (Issa, 1986) using 3 correctors. The flow is considered to be laminar. The motion of the device is captured using OpenFOAM's `sixDoFRigidBodyMotion` library, which uses a deforming mesh approach based on the spherical linear interpolation (SLERP) algorithm (Shoemake, 1985), and the Newmark method (Newmark, 1959) to determine the instantaneous position of a rigid device. For numerical stability, an acceleration relaxation of 0.9 is applied. The mooring is modelled as a restraint by calculating the force based on

Hooke's law and applying an additional acceleration to the system using Newton's Second Law.

3.1. Wave Generation

The data supplied from the experimental campaign is surface elevation time series' at a finite number of spatial locations, obtained using wave gauges. Wave generation has been achieved using the `combinedWaves` functionality from the waves2Foam toolbox (Jacobsen *et al.*, 2012), which allows the free surface and velocity profiles at the inlet boundary to be calculated using linear superposition of N wave components. Here, the number of wave components are selected using Fast Fourier Transform (FFT) analysis of the time series obtained from the wave gauge furthest upstream in the empty tank experimental data. Due to present limitations of the `combinedWaves` functionality (Brown *et al.*, 2019), N is optimised to be the minimum number of components (see Brown *et al.* (2020) for further details) that achieves a user defined tolerance (and is limited to 100 components for numerical stability). These components are selected by systematically including the next wave frequency with the largest amplitude until the 2% tolerance is satisfied, with respect to the experimental data, for the cross correlation coefficient, as well as maximum and minimum surface elevation. This leads to 53, 81 and 100 wave components being used for simulating Wave 1, Wave 2 and Wave 3, respectively, and the components used are presented in Figure 2.

The wave generation methodology used here only guarantees that the signal will be within the specified tolerance at the inlet boundary, and not necessarily elsewhere in the numerical domain. Furthermore, the use of linear superposition neglects higher harmonics and hence the approach is expected to become increasingly inaccurate for highly nonlinear waves (i.e. high wave steepnesses). Therefore, empty tank simulations (Section 4.2) are required to assess the numerical accuracy at the focused location.

3.2. Numerical Setup

The numerical model is setup to represent a section of physical experiments in the COAST laboratory's Ocean Basin at the University of Plymouth (CCP-WSI, 2019). Following the experimental setup, the water depth is set to 3 m, the waves are generated using the approach described above and propagate in the positive x direction (Figure 3). A numerical domain of length 25 m ($0 \leq x \leq 25$ m), width 15.5 m ($-7.75 \leq y \leq 7.75$ m) and height 6 m ($-3 \leq z \leq 3$ m) is used for all simulations, with the still water level located at $z = 0$ (Figure 3). The discretisation in the free surface region ($|z| \leq 0.75$ m) is set to $\Delta z = 0.025$ m (Figure 3a), determined using a mesh convergence study as detailed later in the paper. A cell aspect ratio of 1 is used in the working region ($x \leq 10$), in the vicinity of the platform ($|y| \leq 1$ m) (Figure 3b). The centre of the model is positioned at $x = 4.25$ and $y = 0$, and is set to the draft observed at equilibrium in the experiments (Table 1), with the mooring assumed to be anchored at (x,y,z) = (4.25,0,-3).

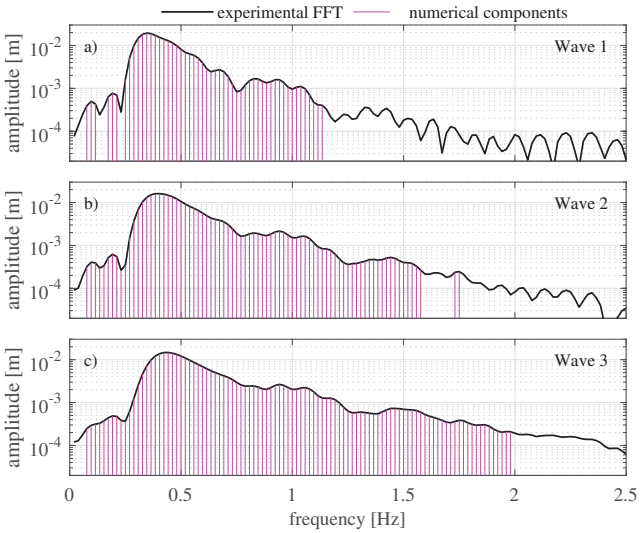

Figure 2. Experimental amplitude spectrum (——) for Wave 1 (a), 2 (b) and 3 (c), and the selected components for the numerical model (——).

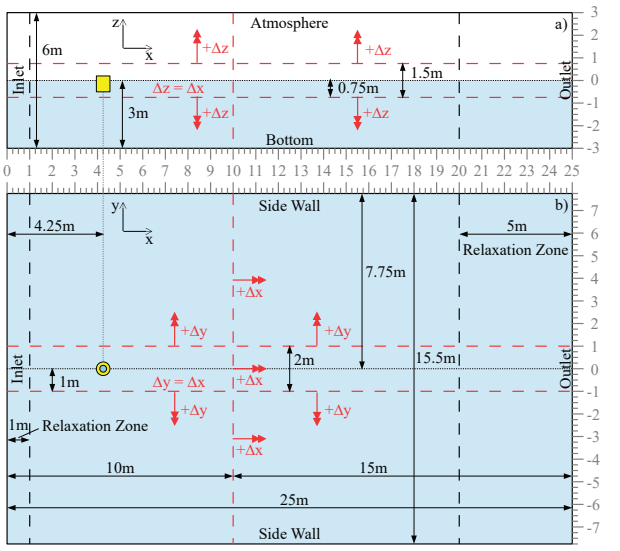

Figure 3. Scale diagram of the numerical setup. Information in red denotes mesh properties with double headed arrows (⇒) showing the direction of increasing mesh grading.

Following the results of CCP-WSI Blind Test Series 1 (Brown *et al.*, 2019; Ransley *et al.*, 2019), it was found that reflections from side and end walls could be negatively influencing reproduction of focused wave events. Hence, in this work the length and width (set to the same as the COAST Ocean Basin) of the domain has been increased substantially to reduce these effects. Furthermore, the relaxation zone technique, included with

the waves2Foam toolbox (Jacobsen *et al.*, 2012), is used to absorb wave reflections, with an inlet relaxation zone of 1 m and an outlet relaxation zone 5 m in length (Figure 3), which is approximately $0.5L_c$ or greater in all cases. The outlet relaxation zone is expected to produce a reflection coefficient of $0.1 - 0.3\%$ for all of the wave conditions considered in this work (Jacobsen *et al.*, 2012).

The necessity for such a large numerical domain makes the case computationally expensive, and hence mesh grading (indicated by double headed arrows, $\twoheadrightarrow$, in Figure 3) is used to mitigate the cost by reducing the number of mesh cells: in the positive $x-$axis the mesh is constant discretisation ($\Delta x = 0.025$ m) for $x \leq 10$ m before linearly increasing to $\Delta x = 0.5$ m; in the y ($|y| > 1$ m) and z ($|z| > 0.75$ m) coordinates, the mesh increases to $\Delta y = \Delta z = 0.25$ m (Figure 3). The structures were meshed using `snappyHexMesh`: Geometry 1 does not require additional mesh refinement around the structure, but Geometry 2 requires two levels of octree refinement (Greaves, 2004) to reproduce correctly. Once the structures are meshed, the mesh size is approximately 11 million cells in both cases.

3.3. Uncertainty Estimations

In order to determine the numerical accuracy, it is essential to also have an understanding for the numerical (and physical) modelling uncertainty. To achieve this, the verification and validation method proposed by Eça and Hoekstra (2014) is utilised, which estimates the order of convergence using a combination of Richardson extrapolation and least squares fitting, and has previously been demonstrated for floating bodies (Eskilsson *et al.*, 2017; Wang *et al.*, 2018). The method requires at least four grids to be considered over a suitably large range of h_i, defined as the characteristic cell size of the i^{th} grid, i.e. $i = 1, 2, \cdots, N$ from finest to coarsest resolution. A brief overview of the method is provided here, with the reader referred to Eça and Hoekstra (2014) for further detail.

The error, ϵ, between the solution for the i^{th} grid (ϕ_i) and the converged value ϕ_0 (i.e. the solution for an infinitely fine grid) is defined as

$$\epsilon = \phi_i - \phi_0 = a h_i^p, \tag{6}$$

where p is the order of convergence and a is a case-specific constant, and can be estimated using Richardson extrapolation

$$\epsilon \approx \delta_{RE} = \frac{\phi_i - \phi_1}{(h_i/h_1)^p - 1}. \tag{7}$$

For simple problems, equations (6) and (7) would suffice to provide a reliable discretisation error estimation. However, in most practical applications there is scatter in the data due to other factors such as iteration error, which potentially leads to values of p which are either too low or too large (Eça and Hoekstra, 2014). Hence it is necessary to introduce additional error estimations which are based on fitting a second order solution, or a combination of first and second order behaviour, respectively:

$$\delta_{RE}^{02} = a_{02} h_i^2, \qquad \delta_{RE}^{12} = a_{11} h_i + a_{12} h_i^2, \tag{8}$$

which will only be used if evaluation with equation (6) is impossible, or unreliable. Furthermore, the above equations can only be utilised for monotonically converging problems, and hence an error ($\delta_{\Delta M}$) based on the observed maximum and minimum values is defined for use in cases which exhibit oscillatory convergence or anomalous behaviour:

$$\delta_{\Delta M} = \frac{\max|\phi_i - \phi_j|}{(h_N/h_1) - 1} \quad \text{for} \quad 1 \leq i, j \leq N. \tag{9}$$

The obtained error can then be converted into uncertainty using a safety factor (Roache, 1997) based on the obtained order of convergence:

$$U_\phi = F_s(p)|\epsilon|. \tag{10}$$

Following Roache (1997), a safety factor of $F_s = 1.25$ is applied for p in the asymptotic range ($0.95 \leq p \leq 2.05$), and $F_s = 3$ otherwise. If the model is converging monotonically the uncertainties are estimated as:

$$U_\phi = \begin{cases} 1.25\delta_{RE} + \sigma & \text{if } p \in [0.95, 2.05] \\ \min(1.25\delta_{RE} + \sigma, 3\delta_{RE}^{12} + \sigma_{12}) & \text{if } p < 0.95 \\ \max(1.25\delta_{RE} + \sigma, 3\delta_{RE}^{02} + \sigma_{02}) & \text{if } p > 2.05 \\ 3\delta_{\Delta M} & \text{if oscillatory convergence} \\ \min(3\delta_{\Delta M}, 3\delta_{RE}^{12} + \sigma_{12}) & \text{if anomalous behaviour} \end{cases} \tag{11}$$

4. Reproduction of Empty Tank Data

In order for CFD to become a robust design tool in the future, it is crucial that the limitations of the tool are well understood. Hence this section aims to quantify the reproduction of the wave profile using the physical empty tank data released at the start of CCP-WSI Blind Test Series 2 (CCP-WSI, 2019). As discussed previously, the predicted motion of the structure was obtained before the release of the experimental data (with the structure in place) and, hence, at the time of submission the accuracy of these results is unknown. Therefore, the problem presented in this work is similar to a scenario that a developer may consider: the wave profile is a known parameter and the unknown response of the device is predicted numerically. Following the release of the full physical dataset, the relationship between the reproduction of the wave and the accuracy of the predicted motion will be discussed further (Section 5).

4.1. Spatial Discretisation and Uncertainty

To determine a suitable mesh resolution for grid independence, each of the three waves were simulated (using the previously determined value of N) using a series of 2D structured meshes with an aspect ratio of 1. These grids used the same x and z dimensions as described above, with resolution ranging from $\Delta x = 0.02$ m ($\approx$

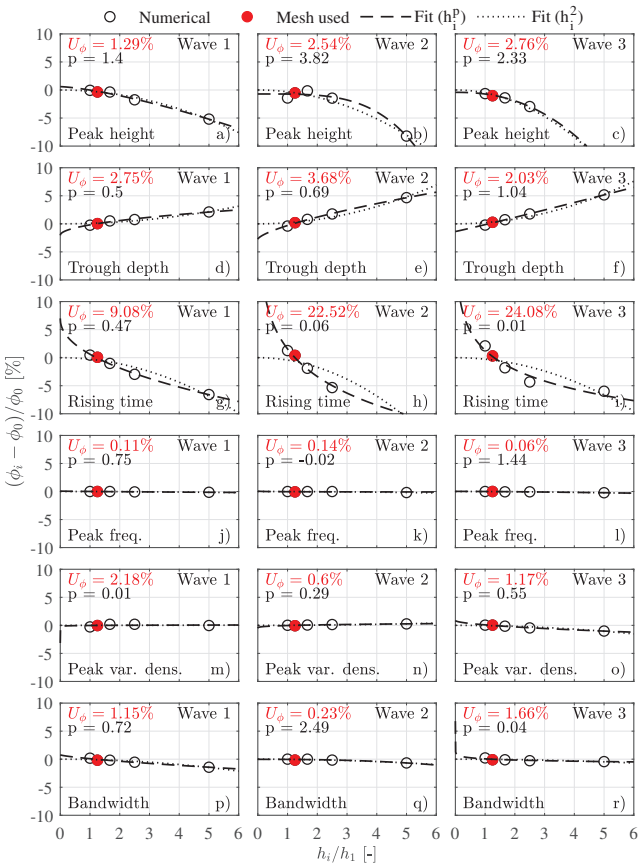

Figure 4. Mesh convergence for Wave 1 (left), Wave 2 (centre) and Wave 3 (right). The chosen mesh (●), uncertainty (U_ϕ), second order fit ($\cdots$), and best fitting p ($- - -$) are also shown.

280k cells) to $\Delta x = 0.1$ m ($\approx$ 11k cells). Defining the refinement ratio as

$$r = \frac{h_i}{h_1} = \sqrt{\frac{N_1}{N_i}} \tag{12}$$

where N_i is the number of cells in the i^{th} mesh, provides a range of $1 \leq r \leq 5$. The convergence of the mesh is determined based on the surface elevation profile at the focus location ($x = 4.25$ m), calculated using a depth integrated approach (Jacobsen *et al.*, 2012). In previous work (Brown *et al.*, 2019), the convergence of the mesh was determined using a single root mean square (RMS) parameter, but here the approach is expanded to consider the six parameters submitted to the CCP-WSI Blind Test Series 2 (Ransley *et al.*, 2020a): peak surface elevation; preceding trough depth; rising time; peak frequency; peak variance density; and bandwidth.

Figure 4 presents the percentage numerical error for Wave 1 (left), Wave 2 (centre) and Wave 3 (right). The six variables of interest are presented: peak height (a,b,c); trough depth (d,e,f); rising time (g,h,i); peak frequency (j,k,l); peak variance density (m,n,o); and bandwidth (p,q,r); along with the best fit for unknown order of convergence ($- - -$) and for second order convergence ($\cdots$). The open markers (○) show the numerical predictions for each of the five mesh considered, and the filled marker (●) the mesh that was used to produce the 'blind' results: the uncertainty (U_ϕ) for the chosen mesh (h_2: $\Delta x = 0.025$ m), and the calculated order of convergence (see Section 3.3), p, is indicated at the top of each plot. In general the variables considered are not in the asymptotic range ($0.95 \leq p \leq 2.05$) likely due to other noise arising from factors such as iteration and rounding errors, but this is accounted for in the larger safety factor applied in these cases (Section 3.3). However, despite being outside the asymptotic range, the uncertainty is generally less than 5% for all variables and hence the chosen mesh is considered to be suitably converged. Rising time is the exception, exhibiting uncertainty up to 25%, indicating that this parameter is the most sensitive to mesh resolution. Therefore, this uncertainty should be taken into account when considering the motion of the structure since it implies a change in steepness that could be influential to the pitch in particular. However, the chosen mesh resolution is considerably finer than that used by Ransley *et al.* (2017), who previously simulated the interaction of a similar focused wave event with a hemi-spherical buoy using a mesh discretisation of 0.037 m in the free surface region, and showed good agreement, indicating that it is suitable level for the present application.

4.2. Error Time Series

Using the numerical setup described in Section 3.2 (which incorporates the conclusions of Section 4.1), simulations are run without the structures in place, to determine the accuracy of the reproduction of the experimental empty tank data. Figure 5 presents the numerical ($\cdots\cdots$) and experimental ($- - -$) surface elevation signals at the focus location, normalised by the amplitude, A_n, for Wave 1 (a), Wave 2 (b) and Wave 3 (c). Also shown (——) is the relative error [%] in the numerical solution, normalised by A_n, along with the RMS ($\mathcal{E}$), error in maximum amplitude (E_p) and cross-correlation coefficient ($\mathcal{C}$) of the two signals. The reproduction of Wave 1 is good ($< 10\%$, $\mathcal{E} \approx 3\%$) throughout, although the larger discrepancies occur after the focus event and are thought to be due to wave reflections in both the numerical and experimental data. Waves 2 and 3 are also largely acceptable ($< 10\%$) and have similar mean error ($\mathcal{E} \approx 3\%$) as Wave 1, but larger spikes can be observed around the main peak, $10 - 20\%$ in magnitude. In the steeper wave (Figure 5c), this is partially due to an asymmetry in the numerical data, leading to an over-prediction before the experimental event, and an under-prediction after. This shows that an amplitude based approach (such as the RMS) can be very sensitive to phase discrepancies and although in this case the majority of the signal is in phase with the experimental data ($\mathcal{C} > 0.99$), a more reliable indicator may be required for future work. Considering just the error in the amplitude of the main peak height (E_p), all three cases are over-estimated, even when taking the uncertainty of 1-3% in the numerical, and 2.5%

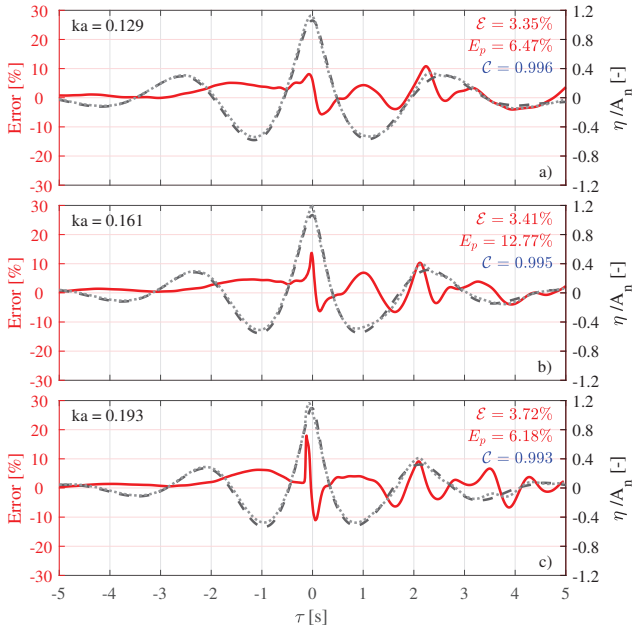

Figure 5. Relative error (——) in the numerical (· · · · · ·) 3D empty tank free surface predictions relative to the experimental data (– – –). Also shown is the RMS error ($\mathcal{E}$), peak amplitude error (E_p) and cross-correlation coefficient ($\mathcal{C}$) of the experimental and numerical signals.

(Ransley *et al.*, 2020a) in the physical into account. The largest error is observed for Wave 2 ($E_p = 12.77\%$), and is substantially less in the other cases ($E_p \approx 6\%$). Having larger peak amplitude error for the middle steepness is slightly surprising but is likely due to premature breaking in the numerical model reducing the wave height in Wave 3, which is consistent with the asymmetric profile in this case. Although the error in peak magnitude is reduced, the overall error in the steepest case is higher (as seen in the value of $\mathcal{E}$) and this highlights the need for multiple criteria when assessing such problems.

5. Post-Release Analysis

At the time of submission, it was thought that the error in the peak motion predictions would be approximately 10% in each degree of freedom (DoF), based on previous experience (Ransley *et al.*, 2017). The confidence in the heave accuracy estimate is relatively high since it is anticipated that it would be similar to the reproduction of the empty tank surface elevation. On the other hand, confidence in the surge and pitch predictions was much lower due to their relationship with the reproduction of surface elevation being less clear, i.e. they are likely to depend on additional parameters such as wave velocity, wave phase and drag, making it harder to estimate error in these cases.

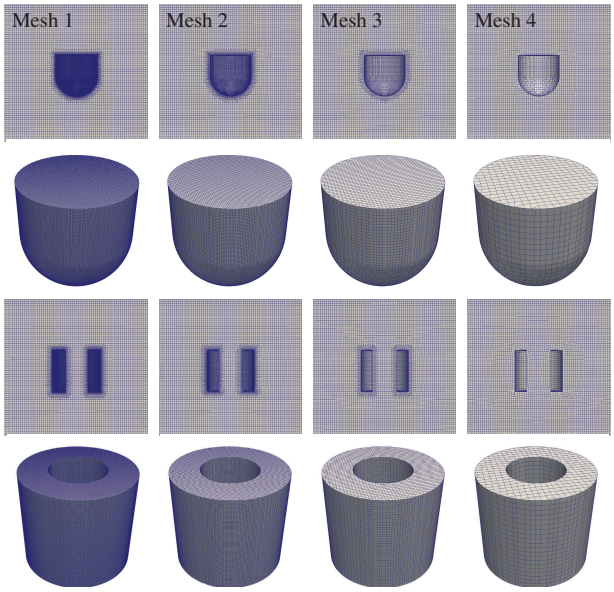

Figure 6. Near geometry resolution for the grids used for mesh convergence and uncertainty calculations.

Following the conclusion of CCP-WSI Blind Test Series 2, the full physical dataset (including the device motion) was released, allowing these 'blind' estimates to be assessed. In this section, the accuracy of the predictions submitted to the Blind Test (Appendix A) is quantified using the released data, considering both the uncertainty due to spatial discretisation and any discrepancy with the physical data. It is observed that the general trends (e.g. over-estimations in surge) in the data are independent of wave steepness. Hence this paper will focus on Wave 1, with the predictions, and corresponding accuracy, for Waves 2 and 3 detailed in Appendix A for reference.

5.1. Uncertainty in Motion Predictions

In the submitted Blind Test results the mesh resolution was determined based on a grid convergence for the wave in an empty tank, but not for the geometry. In this section, the uncertainty in the predicted motion of the structure is assessed using a grid convergence study for the near-structure mesh resolution. To improve the computational efficiency, the simulation size has been reduced for this mesh convergence study by introducing a symmetry plane at $y = 0$ and constraining the motion to three DoFs: surge, heave and pitch. Running on half the resource (64 CPU cores), the simulations ran in approximately 25 hrs (1600 cpu hrs) saving more than half the computational time (Appendix A) with very minor changes in the results ($< 0.5\%$). The simulations were run on a series of grids with increasing mesh resolution in the near vicinity of the device (Figure 6: Meshes 4 and 2 were used for Geometry 1 and 2, respectively), without altering the mesh discretisation in the rest of the domain (i.e. the mesh resolution is

Geometry		1	1	1	2	2	2
DoF		$\boldsymbol{X}_x$	$\boldsymbol{X}_z$	$\boldsymbol{R}_y$	$\boldsymbol{X}_x$	$\boldsymbol{X}_z$	$\boldsymbol{R}_y$
ϕ_{max}	[%]	**10.2**	1.02	3.27	0.45	0.1	**8.44**
ϕ_{min}	[%]	**13.7**	**5.69**	**9.70**	2.95	3.89	0.98
ϕ_{rt}	[%]	0.25	1.27	4.00	0.19	0.53	2.16
ϕ_{fp}	[%]	2.94	1.28	0.70	2.28	1.04	**9.97**
ϕ_{vp}	[%]	**9.37**	0.53	**7.72**	1.05	1.02	**12.2**
ϕ_{bw}	[%]	1.05	**6.31**	1.13	**15.6**	4.62	**8.86**

Table 3. Uncertainty in each parameter supplied to the blind test: Peak value (ϕ_{max}); preceding minimum (ϕ_{min}); rising time (ϕ_{rt}); peak frequency (ϕ_{fp}); peak variance density (ϕ_{vp}); and bandwidth (ϕ_{bw}) of the surge ($\mathbf{X}_x$), heave ($\mathbf{X}_z$) and pitch ($\mathbf{R}_y$) DoFs.

as described previously). The mesh resolution is varied using octree refinement, and the characteristic mesh size is determined by

$$r = \sqrt{\frac{F_1}{F_i}} \tag{13}$$

where F_i is the number of faces over the surface of the geometry for the i^{th} mesh.

Following the uncertainty procedure used for the wave surface elevation (Sections 3.3 and 4.1) the uncertainty in the parameters submitted to the CCP-WSI Blind Test Series 2 (Ransley *et al.*, 2020a) are quantified: Peak value (ϕ_{max}); preceding minimum (ϕ_{min}); rising time (ϕ_{rt}); peak frequency (ϕ_{fp}); peak variance density (ϕ_{vp}); and bandwidth (ϕ_{bw}) of the surge ($\mathbf{X}_x$), heave ($\mathbf{X}_z$) and pitch ($\mathbf{R}_y$) DoFs. Table 3 presents the uncertainty in each of these parameters, and highlights the values higher than 5%. The uncertainty in the parameters for Geometry 2 surge and heave DoFs is generally less than 5%, which is considered to be an acceptable level. Geometry 1, on the other hand, has considerably larger uncertainty in the surge DoF, which could be due to a combination of the coarser mesh used and other numerical errors such as iteration. Hence, a finer mesh is likely required in the vicinity of the structure to reduce uncertainty for this geometry (see Section 5.3). The predictions in the pitch DoF are higher for both structures (7-10%): Geometry 2 in particular has considerable uncertainty for all of the frequency domain parameters. This is due to a double peak in the pitch variance density spectrum (Figure 7l) which is not apparent in the numerical model for the coarser meshes, and starts to develop for the higher mesh resolutions.

It is worth noting that only the numerical uncertainty has been assessed in this work, and that another key consideration is the uncertainty associated with the experimental procedure. It is important to understand the magnitude of both sources of uncertainty in order to determine whether the numerical lies within an acceptable tolerance of the physical data. In this study the repeatability of the signal have been released (Ransley *et al.*, 2020b), stated as a maximum relative standard deviation of 0.3%, 1.2% and 1.8% for heave, surge and pitch, respectively. However, there will undoubtedly be other sources of uncertainty; Ransley *et al.* (2020a) acknowledge that there are likely to be inaccuracies in the measurement of the pitch moment of inertia, which was obtained via a 'swing test' methodology. Since moment of inertia is a key input parameter for most numerical models this leads to some uncertainty when comparing the predicted rotational motion to the physical data. The sensitivity of OpenFOAM predictions to the pitch moment of inertia has been evaluated in another study (Windt *et al.*, 2020) conducted as part of the Blind Test, and showed that $\pm 10\%$ error in the moment of inertia could change the error in the numerical prediction by up to 70%. Therefore, this uncertainty needs to be taken into account when comparing the physical and numerical pitch results, and this may explain any large discrepancies that are observed in this degree of freedom.

5.2. Accuracy of Motion Predictions

Now, following the release of the experimental data (Ransley *et al.*, 2020a), the numerical model's accuracy is evaluated and compared with the previous 'blind' estimate (based on the reproduction of empty tank data). A comparison of the numerical ($- - -$) and experimental (——) surge (a,g), heave (c,i) and pitch (e,k) is presented in Figure 7 for Geometry 1 (a,c,e) and Geometry 2 (g,i,k) in Wave 1 ($ka = 0.129$). The numerical prediction for surge follows a similar trend as the experimental for both geometries ($\mathcal{C} > 0.94$) although the mean drift appears to be over-estimated. This can be observed in the variance density spectra (Figure 7b,h), in which the experimental and numerical are very similar other than at low frequencies where the latter is substantially larger. This over-estimation leads to peak height errors of $E_p = 13 - 15\%$ and RMS errors of $\mathcal{E} = 11 - 13\%$. The peak height errors are larger than the blind estimate ($E_p \approx 10\%$). Since this blind estimate was based on previous experience with a similar structure, this could imply that the accuracy of the numerical model is case sensitive, which is backed up by the errors observed for the other two waves in this work (Appendix A), since there is an increase in error with wave steepness and Geometry 2 is larger than Geometry 1. However, the error in Wave 1 ($ka = 0.129$) is still higher than presented by Ransley *et al.* (2017), who considered a hemi-spherical bottom buoy (i.e. similar to Geometry 1) in a steeper wave ($ka = 0.149$). Assuming the same trend of increasing error with wave steepness, this indicates that the present approach is less accurate, although it should be noted that there is substantial uncertainty for Geometry 1 (Table 3) which needs to be addressed in order to draw any firm conclusions (see Section 5.3).

The heave predictions (Figure 7c,i) are good, as indicated by the low RMS ($\mathcal{E} = 3 - 5\%$) and high correlation ($\mathcal{C} > 0.97$). The numerical variance density spectrum (Figure 7d,j) is also comparable to the experimental spectrum, predicting a similar peak

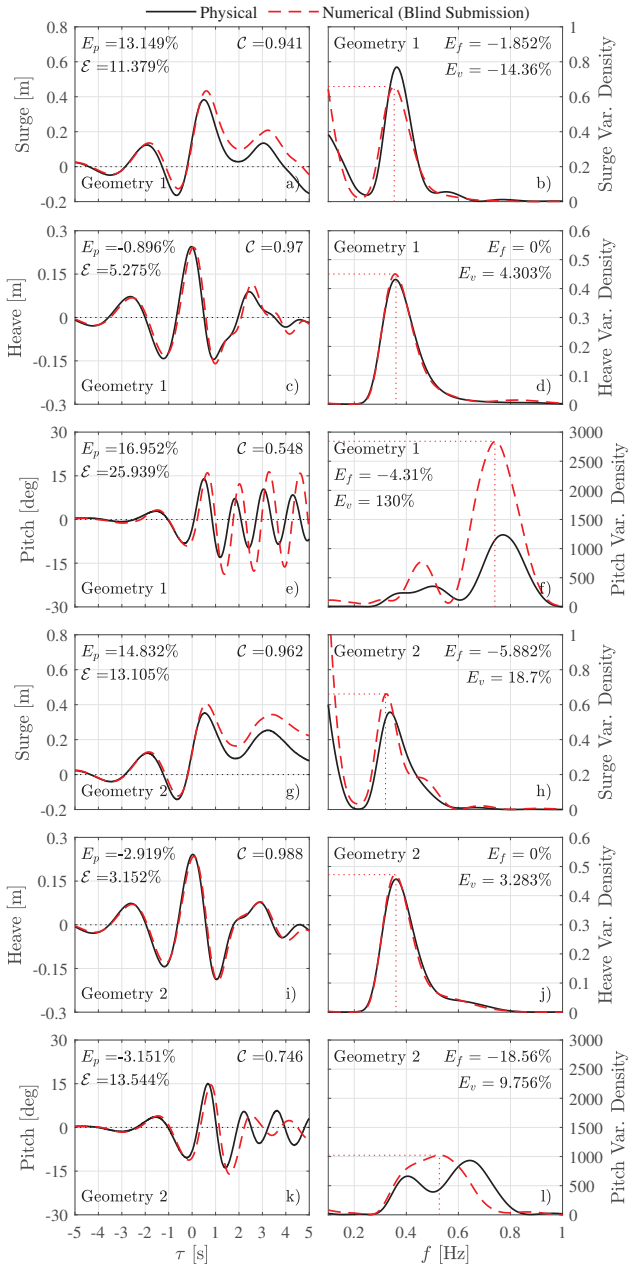

Figure 7. Comparison of the 'blind' numerical (– – –) and experimental (——) motion (left) and variance density spectra (right) in Wave 1. The RMS error ($\mathcal{E}$), cross correlation ($\mathcal{C}$) and errors in peak value (E_p); peak frequency (E_f); and peak variance density (E_v) are also indicated.

frequency, although the peak variance density is over-estimated ($E_v \approx 4\%$). Despite this over-estimation at the peak frequency, the largest peak height is captured well, although it is slightly under-estimated ($|E_p| < 3\%$) and occurs marginally later than observed in the experiments. Interestingly, this discrepancy is lower than the reproduction of the wave (6.5%). This is consistent with the present authors observations for CCP-WSI Blind Test 3 (Brown *et al.*, 2020), where the same geometries were simulated but wave steepness was varied through alterations in amplitude not peak frequency (Ransley *et al.*, 2020b). However, Ransley *et al.* (2020b) showed that there was a near-linear relationship between the RMS error of the surface elevation and heave predictions when considering all participants submissions to the Blind Test, and this backs up the blind hypothesis for the heave DoF.

The numerical predictions for pitch (Figure 7e,f) show much larger discrepancies. For Geometry 1, the predicted peak is substantially larger than observed in the experiments ($E_p \approx 17\%$), indicating that this parameter is not captured well by the numerical model, even if the uncertainty of both numerical and experiment results (3.3% and 1.8%, respectively) are taken into consideration. However, there was also substantial uncertainty in the rising time for the wave (Section 4.1), which could be influential and hence numerical error must be reduced in future work in order to accurately quantify the performance of the model. The pitch natural frequency predicted by OpenFOAM is also slightly lower than observed in the experiments and this leads to substantial RMS error ($\mathcal{E} = 25.939\%$) and low correlation ($\mathcal{C} = 0.548$), which can also be observed ($E_v = 155\%$, $E_f = -1.7\%$) in the variance density spectra (Figure 7f).

The numerical predictions also imply that Geometry 2 has much higher pitch damping than Geometry 1, and this is verified by the experimental data. In general the reproduction of the pitch motion seems substantially better for Geometry 2 than Geometry 1 as indicated by the RMS error ($\mathcal{E} = 13.544\%$) and correlation ($\mathcal{C} = 0.746$). However, the experimental variance density spectrum for pitch shows two distinct peaks, whereas the numerical exhibits only one which lies in the middle of the two experimental peaks. This is likely due to inadequate capture of piston or sloshing effects arising from the moonpool (Molin, 2001; Faltinsen *et al.*, 2007), and may require a substantially finer mesh in order to model accurately, as implied by the mesh convergence study used to quantify the uncertainty (Section 5.1).

5.3. Post-Release Simulations (Non-Blind)

The results presented and analysed in Section 5.2 (and Appendix A) were produced 'blind', i.e. without access to the experimental data with the structures in place. Following the conclusion of CCP-WSI Blind Test Series 2, further simulations have been run (non-blind) to assess the cause of some of the discrepancies seen in Section 5. For computational efficiency, a symmetry plane is introduced at $y = 0$ for all simulations in this section, and motion is constrained to surge, heave and pitch.

5.3.1. Turbulence Modelling

Windt *et al.* (2019a) analysed the effect of using a turbulence model for the CCP-WSI Blind Test Series 2 cases, finding variations in

the surge and pitch peak values of -2% and 1.2%, respectively compared with a laminar model. Using the original mesh described in Section 3.2 (with minor adjustments around the structure to ensure $y^+ < 200$), simulations are run using the $k-\omega$ SST turbulence closure model (Menter, 1994). The results show a change of -3.8%, -0.7% and 2.1% in peak surge, heave and pitch, respectively, compared with the original results. These changes are all slightly larger than observed by Windt *et al.* (2019a), thought to be due to the differences in numerical setup, and are substantial enough to be considered further.

5.3.2. Numerical Domain and Mesh

The mesh resolution for Geometry 1 is now increased, so that it has the same resolution as Geometry 2 (Mesh 2, Figure 6). By doing this, the uncertainty in the results reduces substantially ($U_\phi < 5\%$, with most parameters $U_\phi < 2\%$) in all parameters, except peak variance density in surge (5.38%) and preceding pitch minimum (8.68%). The size of the refinement around the structure has also been increased to 0.1 m from the edge of the structure, to help capture flow around the device and in the moonpool. Using these new meshes, and modelling turbulence with the $k-\omega$ SST model, the new results (Figure 8) show substantial improvements in the surge profiles ($E_p \approx 2\%$ and 8% for Geometry 1 and 2, respectively; $\mathcal{E} \approx 6\%$ for both structures). The heave and pitch DoFs are less affected by the change, and for the latter, it is clear that further work is required to understand the cause of the discrepancies.

6. Conclusions

Numerical simulations of focused wave interactions with simplified floating WECs using the open source CFD software, OpenFOAM, have been presented as part of a contribution to the CCP-WSI Blind Test Series 2. Using empty tank data released by the CCP-WSI working group (CCP-WSI, 2019), the reproduction of three focused wave events is shown to be good (RMS error $\mathcal{E} \approx 3\%$) in general, although the peak magnitude is consistently over-estimated. With the structures in place, the accuracy of the heave predictions is shown to be similar to the reproduction of the waves, but the discrepancies in surge and pitch are substantially higher. This is likely due to a combination of numerical modelling errors that need further assessment in future work.

Following the conclusion of the Blind Test, further simulations were conducted using a different mesh layout and turbulence model, showing substantial improvement in the predictions of surge. This highlights one of the drawbacks of CFD for WSI applications: there are a substantial number of parameters, techniques and user preferences which influence simulation results, and very few established best practices. In the absence of physical data, this leads to considerable uncertainty (and variability) in results. Therefore, future effort needs to be made to standardise the CFD procedure for WSI application in order to improve confidence in the results.

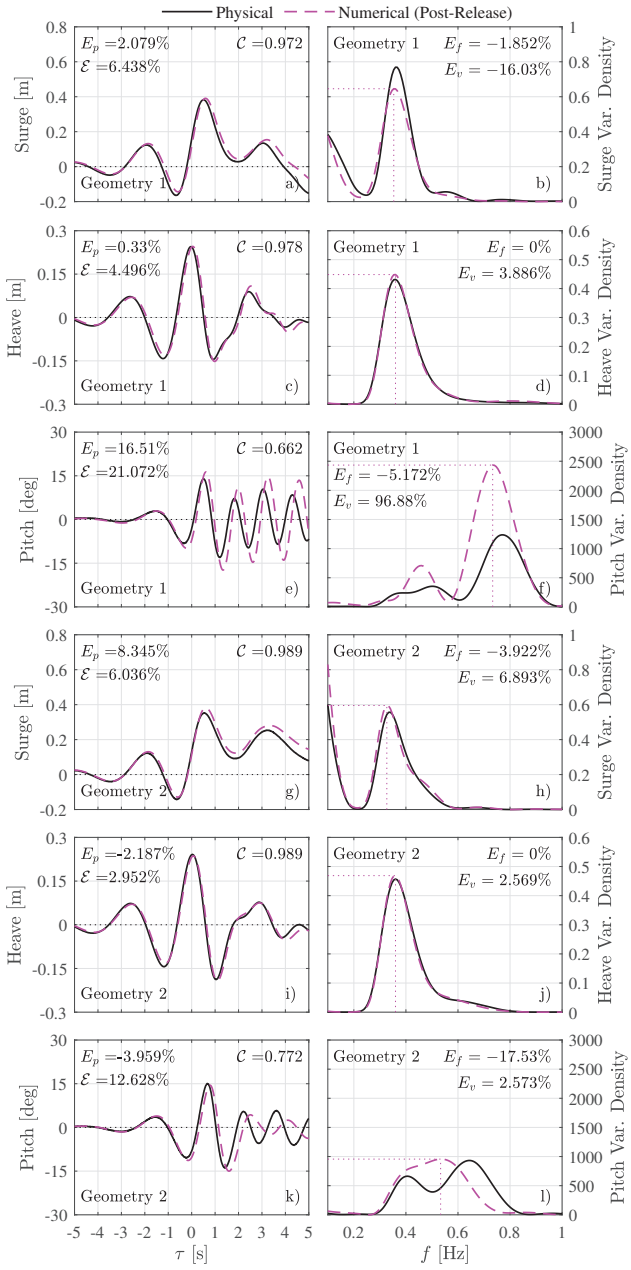

Figure 8. Comparison of the post-release numerical (– – –) and experimental (——) motion (left) and variance density spectra (right) in Wave 1. The RMS error ($\mathcal{E}$), cross correlation ($\mathcal{C}$) and errors in peak value (E_p); peak frequency (E_f); and peak variance density (E_v) are also indicated.

7. Acknowledgements

The presented numerical work has been funded by the Engineering and Physical Sciences Research Council (EPSRC) via the Partnership for Research in Marine Renewable Energy (EP/P026109/1) and Supergen ORE Hub (EP/S000747/1). The

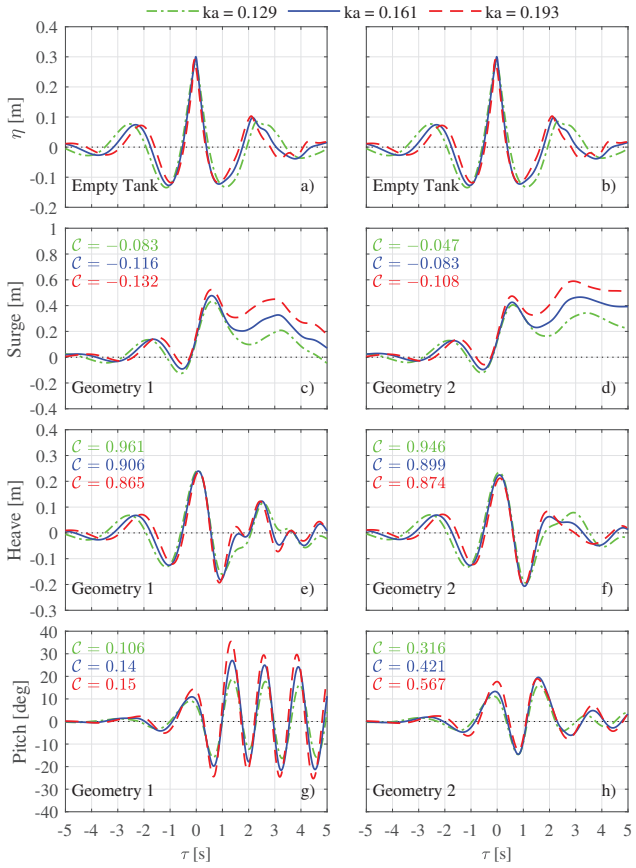

Figure 9. Numerical predictions for $ka = 0.129$ (– · –), $ka = 0.161$ (——) and $ka = 0.193$ (– – –). The empty tank surface elevation signal (a,b), surge (c,d), heave (e,f) and pitch (g,h) are presented for Geometry 1 on the left (a,c,e,g) and Geometry 2 on the right (b,d,f,h). The cross-correlation coefficient ($\mathcal{C}$) of each parameter and the empty tank surface elevation data is indicated in the corresponding colour.

physical data presented here was generated as part of the EPSRC funded CCP-WSI project (EP/M022382/1) and is distributed via the CCP-WSI project website (http://www.ccp-wsi.ac.uk/) as Test Case 004.

REFERENCES

Brown S, Greaves D, Magar V and Conley D (2016) Evaluation of turbulence closure models under spilling and plunging breakers in the surf zone. *Coast. Eng.* **114**: 177–193.

Brown S, Musiedlak PH, Ransley E and Greaves D (2019) Quantifying the predictive capability of OpenFOAM 4.1: Focused wave interactions with a fixed FPSO. *International Journal of Offshore and Polar Engineering* **29(2)**: 158–164.

Brown S, Musiedlak PH, Ransley E and Greaves D (2020) Quantifying the predictive capability of OpenFOAM 5.0: Focused wave impacts with floating bodies. *International Journal of Offshore and Polar Engineering* **30(1)**: 20–27.

CCP-WSI (2019) Focused wave interactions with floating structures (CCP-WSI Blind Test Series 2). https://www.ccp-wsi.ac.uk/blind_test_series_2.

Devolder B, Stratigaki V, Troch P and Rauwoens P (2018) CFD simulations of floating point absorber wave energy converter arrays subjected to regular waves. *Energies* **11**: 641–663.

Eça L and Hoekstra M (2014) A procedure for the estimation of the numerical uncertainty of CFD calculations based on grid refinement studies. *Journal of Computational Physics* **262**: 104–130.

Eskilsson C, Palm J and Bergdahl L (2017) On numerical uncertainty of VOF-RANS simulations of wave energy converters through v & v technique. In *Proceedings of the 12th European Wave and Tidal Energy Conference*, Cork, Ireland, p. 18.

Faltinsen OM, Rognebakke OF and Timokha AN (2007) Two-dimensional resonant piston-like sloshing in a moonpool. *Journal of Fluid Mechanics* **575**: 359–397.

Greaves DM (2004) A quadtree adaptive method for simulating fluid flows with moving interfaces. *Journal of Computational Physics* **194**: 35–56.

Issa RI (1986) Solution of the implicitly discretised fluid flow equations by operator-splitting. *Journal of Computational Physics* **62(1)**: 40–65.

Jacobsen NG, Fuhrman DR and Fredsøe J (2012) A wave generation toolbox for the open-source CFD library: OpenFOAM®. *International Journal for Numerical Methods in Fluids* **70**: 1073–1088.

Menter FR (1994) Two-equation eddy-viscosity turbulence models for engineering applications. *AIAA Journal* **32(8)**: 1598–1605.

Molin B (2001) On the piston and sloshing modes in moonpools. *Journal of Fluid Mechanics* **430**: 27–50.

Newmark NM (1959) A method of computation for structural dynamics. *Journal of the Engineering Mechanics Division* **85(3)**: 67–94.

Palm J, Eskilsson C, Paredes GM and Bergdahl L (2016) Coupled mooring analysis for floating wave energy converters using CFD: formulation and validation. *International Journal of Marine Energy* **16**: 83–99.

Ransley E, Brown S, Hann M, Greaves D, Windt C, Ringwood J, Davidson J, Schmitt P, Yan S, Wang JX, Wang JH, Ma Q, Xie ZH, Giorgi G, Hughes J, Williams A, Masters I, Lin Z, Chen H, Qian L, Ma Z, Causon D, Mingham C, Chen Q, Ding H, Zang J, van Rij J, Yu Y, Tom N, Li Z, Bouscasse B, Ducrozet G and Bingham H (2020a) A blind comparative study of focused wave interactions with floating structures (CCP-WSI Blind Test Series 2). *Proceedings of the Institution of Civil Engineers - Engineering and Computational Mechanics* **in press**.

Ransley E, Greaves D, Raby A, Simmonds D and Hann M (2017) Survivability of wave energy converters using CFD. *Renewable*

Energy **109**: 235–247.

Ransley E, Yan S, Brown S, Hann M, Graham D, Windt C, Schmitt P, Davidson J, Ringwood J, Musiedlak PH, Wang J, Wang J, Ma Q, Xie Z, Zhang N, Zheng X, Giorgi G, Chen H, Lin Z, Qian L, Ma Z, Bai W, Chen Q, Zang J, Ding H, Cheng L, Zheng J, Gu H, Gong X, Liu Z, Zhuang Y, Wan D, Bingham H and Greaves D (2020b) A blind comparative study of focused wave interactions with floating structures (CCP-WSI Blind Test Series 3). *International Journal of Offshore and Polar Engineering* **30(1)**: 1–10.

Ransley E, Yan S, Brown S, Mai T, Graham D, Ma Q, Musiedlak PH, Engsig-Karup A, Eskilsson C, Li Q, Wang J, Xie Z, Sriram V, Stoesser T, Zhuang Y, Li Q, Wan D, Chen G, Chen H, Qian L, Ma Z, Mingham C, Causon D, Gatin I, Jasak H, Vukčević V, Downie S, Higuera P, Buldakov E, Stagonas D, Chen Q, Zang J and Greaves D (2019) A blind comparative study of focused wave interactions with a fixed FPSO-like structure (CCP-WSI Blind Test Series 1). *International Journal of Offshore and Polar Engineering* **29(2)**: 113–127.

Roache P (1997) Quantification of uncertainty in computational fluid dynamics. *Annual Review of Fluid Mechanics* **29**: 123–160.

Rusche H (2002) *Computational fluid dynamics of dispersed two-phase flows at high phase fractions*. PhD thesis, Imperial College of Science, Technology & Medicine.

Schmitt P, Doherty K, Clabby D and Whittaker T (2012) The opportunities and limitations of using CFD in the development of wave energy converters. In *International Conference on Marine and Offshore Renewable Energy*, London, UK, pp. 1–9.

Shoemake K (1985) Animating rotation with Quarternion curves. *ACM SIGGRAPH Computer Graphics* **19**: 245–254.

Wang W, Wu M, Palm J and Eskilsson C (2018) Estimation of numerical uncertainty in computational fluid dynamics simulations of a passively controlled wave energy converter. *Proceedings of the Institution of Mechanical Engineers, Part M: Journal of Engineering for the Maritime Environment* **232**: 71–84.

Weller H, Greenshields C, Bainbridge W, Janssens M and Santos B (2017) OpenFOAM 5.0. https://openfoam.org/release/5-0/.

Windt C, Davidson J, Akram B and Ringwood J (2018a) Performance assessment of the overset grid method for numerical wave tank experiments in the OpenFOAM environment. In *Proceedings of the ASME 37th International Conference on Ocean, Offshore and Arctic Engineering*, Madrid, Spain, p. 10.

Windt C, Davidson J and Ringwood J (2018b) High-fidelity numerical modelling of computational fluid dynamics-based numerical wave tanks. *Renewable and Sustainable Energy Reviews* **93**: 610–630.

Windt C, Davidson J, Schmitt P and Ringwood J (2019a) Contribution to the CCP-WSI Blind Test Series 2: CFD-based numerical wave tank experiments employing an impulse source wave maker. In *Proceedings of the 13th European Wave and Tidal Energy Conference*, Naples, Italy, p. 10.

Windt C, Davidson J, Schmitt P and Ringwood J (2019b) On the assessment of numerical wave makers in CFD simulations. *Journal of Marine Science and Engineering* **7**: 47–91.

Windt C, Davidson J, Schmitt P and Ringwood J (2020) Wave–structure interaction of wave energy converters: A sensitvity analysis. *Proceedings of the Institution of Civil Engineers - Engineering and Computational Mechanics* **in review**.

A. Blind Test Submission

For reference, this section presents the data that was submitted to the CCP-WSI Blind Test Series 2, and was produced without access to the physical data with the structures in place. Figure 9 presents a comparison of the numerical time series (5 seconds either side of the focus time, t_f) for $ka = 0.129$ (– · –), $ka = 0.161$ (——) and $ka = 0.193$ (– – –). The empty tank surface elevation signal (a,b), surge (c,d), heave (e,f), and pitch (g,h) are presented for Geometry 1 on the left (a,c,e,g) and Geometry 2 on the right (b,d,f,h). The corresponding error, with respect to the released physical data, in each case is presented in Table 4. Error in surge ($\boldsymbol{X}_x$), heave ($\boldsymbol{X}_z$), and pitch ($\boldsymbol{R}_y$) are presented, considering a number of criteria: peak height (E_p), peak variance density (E_v), peak frequency (E_f), RMS ($\mathcal{E}$) and cross-correlation ($\mathcal{C}$). The

Geometry			1	1	1	2	2	2
Wave			1	2	3	1	2	3
$\boldsymbol{X}_x$	E_p	[%]	13.2	15.5	20.7	14.8	23.9	28.4
	E_f	[%]	-1.9	-1.7	14.5	-1.8	-28.4	2.8
	E_v	[%]	-16.8	-30.7	-11.3	11.5	26.0	27.5
	$\mathcal{E}$	[%]	11.4	17.7	22.7	13.1	17.4	15.7
	$\mathcal{C}$	[−]	0.94	0.89	0.89	0.96	0.96	0.99
$\boldsymbol{X}_z$	E_p	[%]	-0.9	-0.2	0.5	-2.9	-2.0	-4.1
	E_f	[%]	0.0	0.0	0.0	-5.9	0.0	0.0
	E_v	[%]	4.0	-1.0	-2.8	4.0	-3.7	-7.3
	$\mathcal{E}$	[%]	5.3	4.6	5.1	3.2	3.4	3.9
	$\mathcal{C}$	[−]	0.97	0.97	0.96	0.99	0.98	0.98
$\boldsymbol{R}_y$	E_p	[%]	17.0	22.2	17.2	-3.2	-8.9	-15.1
	E_f	[%]	-1.7	-1.7	-1.7	-17.2	-20.6	-13.2
	E_v	[%]	154.7	95.1	78.8	8.1	51.9	91.5
	$\mathcal{E}$	[%]	25.9	21.3	20.0	13.5	14.7	14.1
	$\mathcal{C}$	[−]	0.55	0.70	0.72	0.75	0.70	0.76

Table 4. Reproduction of experimental data for each case: Error in peak height (E_p); peak frequency (E_f); peak variance density (E_v); RMS error ($\mathcal{E}$); and cross correlation ($\mathcal{C}$) are presented for surge ($\boldsymbol{X}_x$), heave ($\boldsymbol{X}_z$) and pitch ($\boldsymbol{R}_y$).

Geometry		1	1	1	2	2	2
Wave		1	2	3	1	2	3
# Cells	[-]	11M	11M	11M	11M	11M	11M
Clock Time	[hrs]	31.1	42.1	52.8	43.3	60.5	78.5
Cores	[-]	128	128	128	128	128	128
Exec. Time	[cpu hrs]	3984	5385	6754	5543	7740	10053
Max Co.	[-]	0.5	0.5	0.5	0.5	0.5	0.5
max δt	[ms]	8.8	13	14	5.6	6.0	5.8
min δt	[ms]	0.3	0.3	0.2	0.1	0.2	0.1
mean δt	[ms]	1.4	1.4	1.4	1.0	0.9	0.9

Table 5. Required computational effort for each case.

presented results were run using the in-house high performance computing service at the University of Plymouth. This facility consists of 52 2U Twin Sq. (4 Nodes) networked with Intel Omni-Path cabling, and equipped with dual Intel E5-2683v4 8 core 2.5 GHz processors with 128 GB of memory per motherboard. Each simulation was run using 128 processors (≈ 86000 cells per processor) and the computational effort required for each case is presented in Table 5. The required clock times range from $30 - 80$ hours ($\sim 4000 - 10000$ CPU hrs), and show an increase with wave steepness. Furthermore, simulations of Geometry 2 are substantially more expensive, which is thought to be a combination of increased mesh resolution on the device, and the modelling of the moonpool region.